HAL open science

Studying of parameters of two-phase displacement in porous media with MRI technique

Jamal Fannir, Irina Panfilova, Sébastien Leclerc, Didier Stemmelen

To cite this version:

Jamal Fannir, Irina Panfilova, Sébastien Leclerc, Didier Stemmelen. Studying of parameters of two-phase displacement in porous media with MRI technique. Mechanics & Industry, 2020, 21 (5), pp.524. 10.1051/meca/2020058 . hal-02921621

HAL Id: hal-02921621

https://hal.univ-lorraine.fr/hal-02921621v1

Submitted on 25 Aug 2020

HAL is a multi-disciplinary open access archive for the deposit and dissemination of scientific research documents, whether they are published or not. The documents may come from teaching and research institutions in France or abroad, or from public or private research centers.

L'archive ouverte pluridisciplinaire **HAL**, est destinée au dépôt et à la diffusion de documents scientifiques de niveau recherche, publiés ou non, émanant des établissements d'enseignement et de recherche français ou étrangers, des laboratoires publics ou privés.

Distributed under a Creative Commons Attribution 4.0 International License

Mechanics & Industry **21**, 524 (2020)
© J. Fannir et al., published by EDP Sciences 2020
https://doi.org/10.1051/meca/2020058

Mechanics & Industry

Available online at:
www.mechanics-industry.org

Scientific challenges and industrial applications in mechanical engineering
Philippe Le Grognec (Guest Editor)

REGULAR ARTICLE

OPEN ACCESS

Studying of parameters of two-phase displacement in porous media with MRI technique

Jamal Fannir*, Irina Panfilova, Sébastien Leclerc, and Didier Stemmelen

LEMTA – UMR 7563 Laboratoire d'Energétique et de Mécanique Théorique et Appliquée, 2 Avenue de la Forêt de Haye, BP90161, 54504 Vandœuvre-lès-Nancy Cedex, France

Received: 10 October 2019 / Accepted: 24 March 2020

Abstract. This study describes experimental research on two-phase flow displacement using Magnetic Resonance Imaging (MRI) techniques. The overall purpose of this investigation is to determine kinetics process of phase trapping during (water-oil) two-phase flow, the front deformation and the phases saturation propagation along a vertical model. In these water flooding experiments, the porous medium model consists of packed beads of polystyrene ($0.4\,\text{mm} < dp < 0.6\,\text{mm}$) or sand grains ($0.02\,\text{mm} < dp < 0.50\,\text{mm}$). In order to conduct high accuracy experiments, a Nuclear Magnetic Resonance (NMR) spectrometer operating at 14 T (corresponding to a 600 MHz ^{1}H resonance) equipped with an imaging device was used. With this equipment we can measure and visualize the two-phase flow in a vertical model of porous medium under ambient conditions. The obtained results have shown that the oil saturation profile is strongly influenced by the material properties such as the phase wetting, the sample porosity and permeability as well as the injection rate. The influence of flow velocity on the residual oil saturation was also studied. The experimental results allow an essential understanding of immiscible fluid displacement in two different types of porous medium that differ from each other mainly by the effects of wettability.

Keywords: MRI / porous media / oil-water displacement / viscous fingering / residual oil

1 Introduction

Two-phase flow in porous media is very important and widely applicable in the petroleum industry (such as estimation of recoverable oil reserve, optimization of the recovery techniques, etc.) but also in the sector of chemical industry (catalytic reactors, separation and extraction) or in the hydrogeology domain (pollution of aquifers by NAPL). This explains the importance of the studies aiming to improve the description of multi-phase flow in porous media. Notably, the simultaneous flow of two immiscible fluids (water-oil) in porous media is not always well described by Darcy's generalized law, which only takes into account water/oil saturation as additional descriptive variable. This has a substantial impact on the description of the two-phase flow stability under the simultaneous effect of the force of gravity, viscosity and superficial tension.

For the study of two-phase flow in porous media, several kinds of imaging methods have been applied including X-ray, computed tomography scanners (CT) [1–3] synchrotron computed micro-tomography [4] and magnetic resonance imaging (MRI) techniques [5–9]. Among these methods, only MRI is able to visualize the internal structure of a system in three dimensions with a spatial resolution of the species present. Furthermore, MRI also allows in-situ measurements of flow velocity, saturation and diffusion–dispersion of the fluid flow within the porous media. Another opportunity of the MRI is that it can be used to probe both microscopic and macroscopic properties.

The rapid development of new quantitative magnetic resonance imaging technologies led to new opportunities with interesting results for measurements of fluid flow in porous media. Johns and Gladden [10] have used MRI technique to visualize the dissolution of entrapped ganglia or "blobs" of octanol within the pore space of a randomly packed bed of glass beads, by a mobile aqueous phase. They also acquired three dimensional images and were able to distinguish the solid, hydrocarbon, and aqueous phases. Finally, they also obtained velocity maps of the mobile aqueous phase. Ersland et al. [11] used the MRI techniques to study how the oil recovery is affected by fractures. They have obtained high spatial resolution images of the water-oil flow inside a 1 mm fracture. Furthermore, in a recent work in LEMTA laboratory, MRI has been employed

* e-mail: Jamal.fannir@univ-lorraine.fr

This is an Open Access article distributed under the terms of the Creative Commons Attribution License (http://creativecommons.org/licenses/by/4.0), which permits unrestricted use, distribution, and reproduction in any medium, provided the original work is properly cited.

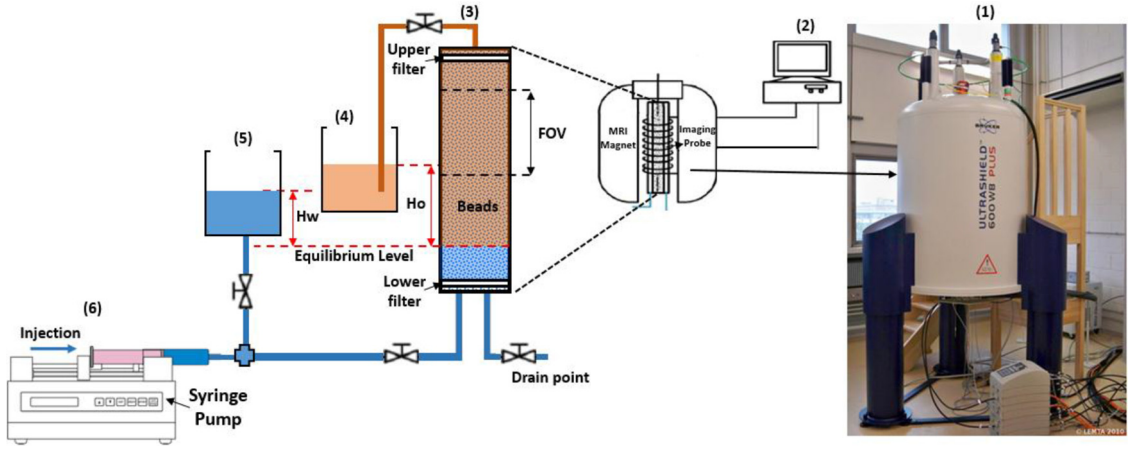

Fig. 1. Experimental setup: (1) 600 MHz NMR system; (2) Computer for data processing; (3) Porous media sample; (4) Oil tank; (5) Water tank; (6) Water injection pump.

for studies of fluid flow within granular porous media [12]. The authors have shown the possibility of visualization of the velocity field in porous media and accurate measurements of interstitial and averaged velocities in packed beds.

The purpose of the present study is the investigation of the immiscible fluid displacement in porous medium. We focus on the wettability properties of the fluids with the solid surfaces as this is an important factor for secondary recovery of hydrocarbons. Furthermore, several types of forces such as capillary, viscous and gravitational are extremely important to describe the two-phase flow. In this project, MRI was used to experimentally examine the water-oil flux through a vertical porous model.

Using MRI technique, we also study the dynamics of the displacement front, its deformation and the phase trapping during the two-phase flow process. Displacement in porous media is characterized by the formation of different structures of the phase distribution in porous space. For the same saturation, the fluids can form different shapes [13]. So, these various shapes can be described by the displacing phase saturation S and additional criteria (such as wettability), responsible for the type of the shape.

2 Experiments

2.1 Experimental system

A scheme of the experimental setup is shown in Figure 1. The setup consists of two parts: the first one is a high resolution 600 MHz MRI spectrometer equipped with a 14 T vertical magnet, shielded gradient coils providing a maximum gradient strength of 450 mT/m and a 40 mm diameter quadrature resonator. With this system we measure and visualize directly the two-phase flow in a vertical model of porous medium (packed beads or sands) under the ambient condition. The MRI technique allows for non-invasive measurements (2D or even 3D mapping) of the concentration of hydrogen nuclei ^{1}H in the liquid phase inside the porous media. These hydrogen nuclei can belong to molecules of water or other liquids. The ^{1}H species associated with water or hydrocarbon provide the phase distribution images, and it is also possible to distinguish the solid and liquid phases.

The second part is the porous medium column. A tube with 34 mm internal diameter and 14 cm in height was filled and compacted with sands or polystyrene beads. The beads are kept inside the tube by two porous filters and two caps. A syringe pump is connected to the system to inject the water upward at constant flow rate. This pump can inject at a very low rate with an accuracy of ±0.5%.

Signal is acquired and processed using the Bruker Paravision software. Further processing is done with the Matlab software.

2.2 Sample material

2.2.1 Porous medium

We have used two different types of materials for tubes and beads according to their wettability. The synthetic porous medium consisted of polystyrene beads or sands with average grain size of 0.5 mm and 0.13 mm respectively. The average estimated porosity measured by the gravimetric method was around 38%, and the intrinsic permeability was calculated using Kozeny-Carman equation for non-consolidated medium:

$$K = \frac{\varphi^3}{36C(1-\varphi)^2} d_p^2 \tag{1}$$

where K is the sample intrinsic permeability, C is the Kozeny-Carman constant (in this study $C = 5$), φ is the sample porosity, and dp is the mean diameter of the grains.

The porous media characteristics for both materials are given in Table 1.

The samples of sand always have different grain sizes even though the grain size spectrum is relatively narrow. Indeed, it is important in our study to determine the average grain size and grain size distribution accurately as it will be used in our calculations and discussion. Therefore, the average grain size of the selected sand was evaluated from grain size populations (not directly from the mass fraction). Table 2 shows the sand particles size distribution

Table 1. The porous media characteristics for polystyrene beads and packed sand.

Porous medium	Model tube material	Porosity (%)	$MnCl_2$ (mol/l)	Permeability (m^2)	Model net length (cm)	Model internal diameter (cm)
Polystyrene beads	Plastic	38	0.01	2.9E–10	10	3.4
Packed Sand	Glass	39	0.02	1.5E–11	10	3.4

Table 2. Sand particles size distribution versus mass and grain population.

Size of sieve (mm)	Average size of population (mm)	Mass (g)	Number of grains (supposed to be spherical)	Frequency (%)
0.025	0.040	0.11	188867	3.614
0.05	0.075	2.82	605232	11.581
0.1	0.130	82.63	3405372	65.159
0.16	0.205	92.75	974786	18.652
0.25	0.325	19.62	51749	0.990
0.4	0.450	0.16	206	0.004

Table 3. Fluids properties at standard condition (20 °C).

Oil density (kg/m^3)	Oil viscosity (cP)	Water density (kg/m^3)	Water viscosity (cP)	σ (N/m)
800	2.96	1000	1	0.05

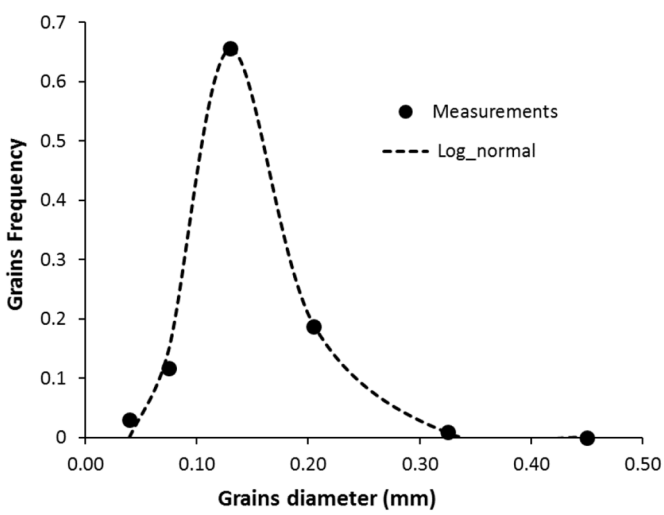

Fig. 2. Sand Grain frequency vs grain size matching with Log-normal function.

as a function of mass. These data were obtained using different available sieves.

Based on the above data, the average sand grain size estimated to be 0.13 mm using a log-normal function (Fig. 2). The value of the permeability shown in Table 1 was calculated from the Kozeny-Carman formula (Eq. (1)) with the estimated average grain size.

2.2.2 Fluids

In all experiments, PTX2000 fuel was used as oil phase, and a solution of water and $MnCl_2$ as displaced phase. Physical properties of these fluids are given by the products data sheet and confirmed in our lab using standard measurements techniques (Tab. 3). The interfacial tension σ between oil and water was assumed to be 0.05 N/m [14].

2.3 Experimental process

As a first step, the sample tube was filled with oil. A vacuum pump is used to remove air in order to obtain fully saturated samples. At initial state, we install a hydrostatic equilibrium of water-oil contact inside of the porous sample which is calculated with the levels of water and oil in tanks (Fig. 1). In doing so the water oil interface is homogeneously distributed near the bottom filter. The injection rate was controlled by the syringe pump. The water solution (distilled water + $MnCl_2$) was injected into the column from below with the objective to prevent the deformation of water-oil interface by the gravity. The volumetric injection flow rate was varied from 0.08 mL/min to 0.16 mL/min and the corresponding superficial velocity was calculated using the geometry and porosity of the model. For each experiment, the MR sequences were performed during more than 10 hours, a period corresponding to the injection of 3 and more pore volumes (PV) of water [15].

2.4 Imaging protocol

The magnetic resonance imaging technique is an effective, non-invasive method for determining fluid saturation in porous media by detecting ^{1}H density. The imaging method used a classical multi-slice spin echo sequence. The MRI echo signal can be described as [5,16]:

$$I(f, T_E) = I_0(f)\left(1 - \exp\left(-\frac{T_R}{T_1}\right)\right)\exp\left(-\frac{TE}{T_2}\right) \quad (2)$$

in which I is the observed intensity of the magnetic signal at resonance frequency f, I_0 is the intrinsic magnetic intensity, T_E is the echo time, T_R is the repetition time, T_1 is the longitudinal relaxation time and T_2 is the transverse relaxation time. The intrinsic magnetic intensity I_0 is in principle proportional to the number of protons ^{1}H. Taking $T_R > 5\,T_1$ and $T_E < T_2/5$, the observed magnetic intensity is close to the intrinsic one, i.e. $I(f, T_E) \approx I_0(f)$ which makes it possible to build an image in ^{1}H density almost independent of the relaxation times.

In this study, the MRI was mainly used to measure the oil signal intensity in each sample and to monitor the oil saturation change during the experimental test. We made sure that the NMR signal is only sensitive to oil. Indeed, both water and oil contain protons ^{1}H and produce NMR signals that are acquired in the same time. For this reason, we added a strong paramagnetic contrast agent (Mn^{2+}) to reduce the relaxation times of the water [16]. By taking an aqueous solution of $MnCl_2$ at 0.01 mol/l, the relaxation decay of the water phase could be greatly reduced: T_2 of water fell from 3 s to below 1 ms. In this way the signal of water disappeared so quickly that it was not possible to image it. However, $MnCl_2$ is not soluble in organic compounds, so there is no effect on the relaxation time of oil (~1 s). Therefore, the signal of oil was the only measured signal. Consequently, instead of using pure water as the injection phase, we used an aqueous solution of $MnCl_2$ with a neglected T_2 time. For the imaging sequences, it is necessary to set the echo time T_E between the transverse relaxation time T_2 of the aqueous solution and the oil (i.e. $T_{2w} \ll TE \ll T_{2o}$) and to take a relatively large repetition time ($T_R \simeq T_{1o}$).

MR images are acquired using a slice selection procedure. By changing the orientation of the magnetic field gradients in the imaging procedure, it is possible to obtain vertical sections along the axis of the sample or horizontal axial sections. Subsequently we realized over time one vertical section (acquisition time about 4 min) followed by 8 horizontal sections (acquisition time also about 4 min).

In this study, the mapping was done with the following acquisition parameters:

- Echo time T_E: 15 ms for polystyrene beads and 5 ms for sand experiments.
- Time of repetition T_R: 1 s.
- Field of View FOV: 50×50 mm^2.
- Imaging matrix: 256×256 pixels with a resolution of 0.19 mm for 1 pixel.
- Slice thickness: 1 mm.

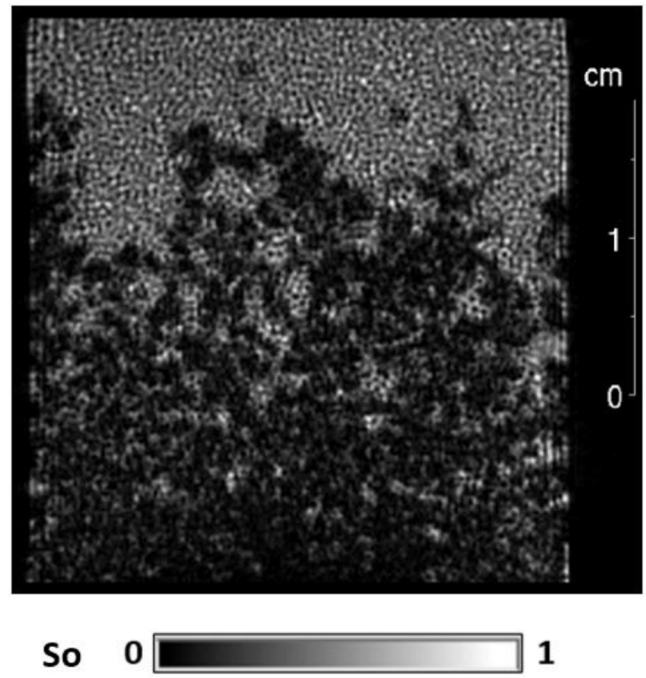

Fig. 3. MRI vertical slice of a stack of polystyrene beads contained in a PVC tube and initially saturated with oil. The aqueous solution of $MnCl_2$ is injected from the bottom with a flow rate of 0.12 mL/min. The image is obtained after 3h45 of water injection. Water saturated regions appear in black and those saturated with oil in white.

The obtained images were satisfactory from the point of view of high spatial resolution, and it is clearly possible to visualize the oil trapping and the dynamic evolution of the two-phase flow (Fig. 3).

From the MR intensity images, the oil saturation can be calculated as following:

$$S_0 = I_i / I_{\text{ref}} \quad (3)$$

where S_0 is the saturation of the oil phase, I_i is the dynamic MR signal intensity at time i, I_0 is the reference MR signal intensity (initial image at oil saturation of 100%). The accuracy of the saturation measurements depends mainly on the signal-to-noise ratio (SNR) of the NMR intensity measurements obtained for each voxel in the image. This SNR itself depends on many factors such as size of the voxel, intensity of the magnetic field, nature of the porous medium, number of repetitions in the MRI sequence, etc. In our case, due to the use of a high field spectrometer (14T), it is of the order of a few percent.

3 Results

The MRI raw data acquired are processed with Matlab software to obtain the visualization of the displacement of the oil by the injected aqueous solution (water + manganese chloride). These images have a resolution of 256×256 pixels for a field of view (FOV) of 5×5 cm^2. The centre of

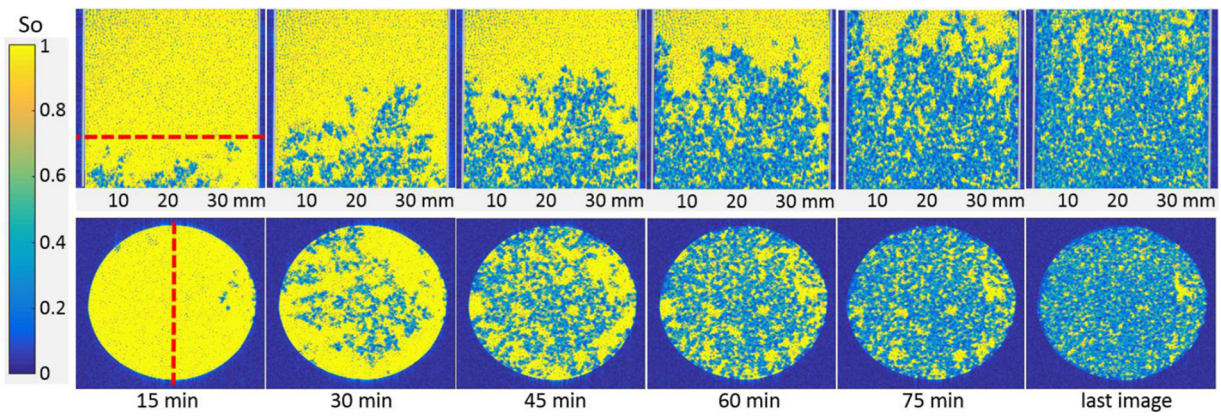

Fig. 4. Consecutive MRI images of the water–oil displacement in the model of polystyrene beads with the injection flow rate of 0.12 mL/min. The oil is yellow and the water is light blue. The acquisition of MRI signal was made each 15 minutes and shown here from the first water appearance in FOV. The dotted line on the first vertical section indicates the position of the horizontal sections (and vice-versa for the horizontal section below).

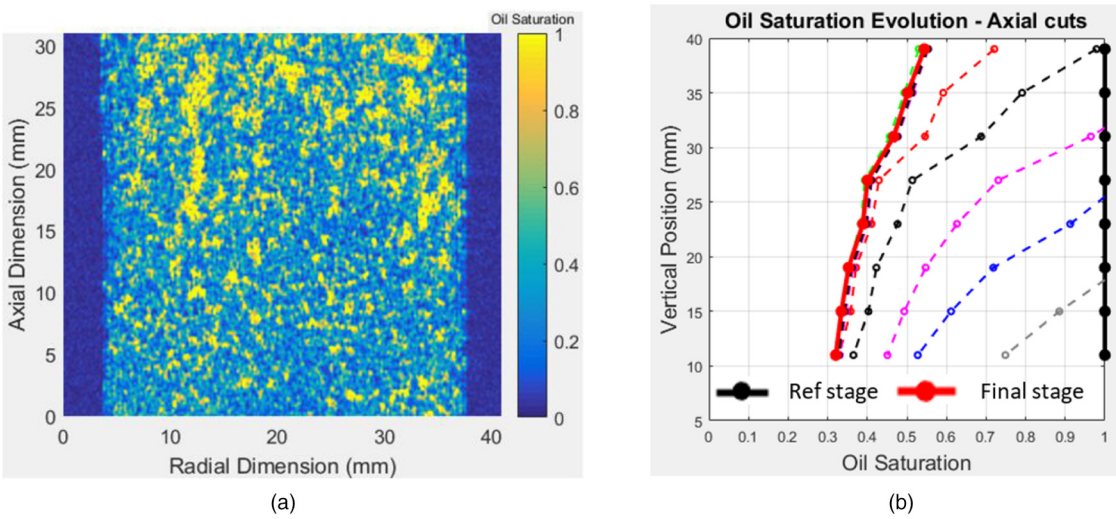

Fig. 5. Residual oil saturation image in a vertical section (a) for the displacement process after the injection of 3.5 PV of the displacing fluid. Time evolution of oil saturation profiles deduced from the 8 axial sections (b).

the FOV for vertical sections is located at 6.7 cm above the lower filter (bottom of the sample). For each model, data are recorded on vertical and horizontal sections with an interval of 15 minutes between each series of images. The recorded data are then processed with Matlab to retrieve the images on which statistical analyzes can be done. To compare the tests at different rates, we introduce the porous volume parameter (PV). It corresponds to the pore volume calculated from the height of the sample imaged by MRI.

3.1 Experiment with a packed polystyrene beads model

Figure 4 shows the consecutive series of images in vertical and horizontal directions, for the experiment of the polystyrene beads model with the injection flow rate of 0.12 mL/min. The acquisition of MRI signal was made each 15 minutes and shown here from the first water appearance in FOV. In this case the first water appears around 3 hours after the start of the water injection.

We note that the displacement of the oil by water does not correspond to a piston-like flow, but generates fingers leading to a trapping of the oil during the two-phase flow. At the end of the displacement process, the total residual oil saturation, averaged through the sample volume, is equal to 38%. Indeed, the residual oil saturation obtained at the end of the process is an average saturation throughout the model, while it is observed that the saturation is not uniformly distributed. It is therefore necessary to observe in detail what happens at each position along of the model.

The analysis of the last image (Fig. 5) where the oil saturation was stabilized, shows an increasing distribution of the residual oil saturation as a function of the vertical position. However, it is easy to observe that the residual oil

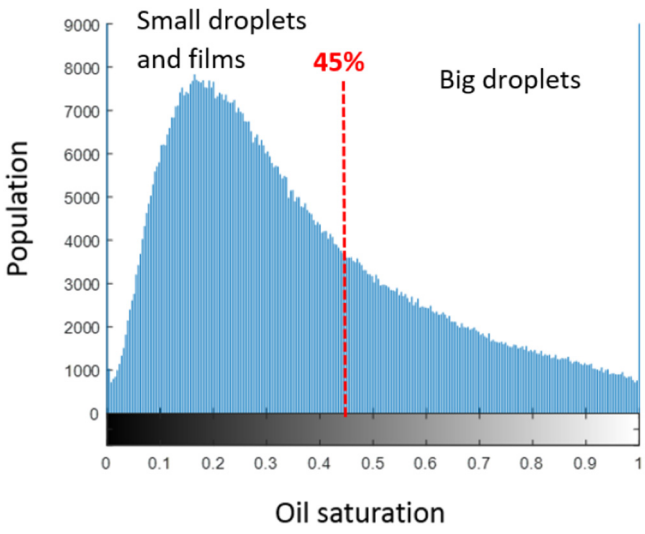

Fig. 6. Histogram of residual oil distribution corresponding to its population in the polystyrene beads model.

saturation is much greater in the higher sections of the model than in the lower ones. These differences are caused by the development of fingerings along the model. We also note that the continuous field of low oil saturation, observed in Figure 5a in light blue colour, corresponds to the oil film left on the surface of the polystyrene beads. The variation of saturation of these zones depends on the thickness of these films and the interactions between oil, water and surface of the beads. Therefore, a distinction was made between these oil films and the oil trapped due to the development of fingerings.

For this test, two types of residual oil were observed. The first type corresponds to the large oil droplets grouped into small discontinuous formations elongated in the direction of flow; the second type of residual oil corresponds to the oil films which cover the oil-wet polystyrene beads.

By studying the small areas in Figure 5a without big oil droplets an oil saturation lower than 45% was observed. The statistical analysis of this experimental test (Fig. 6) shows that the oil saturation population under 45% is equivalent to around two-third of total residual oil saturation, which was trapped in the form of thin films and small droplets due to hydrophobic behaviour of the bead surface.

The estimated oil saturation for large oil droplets (Fig. 5a) is in the range from 45% to 100%. It represents approximately the last one-third of residual oil (Fig. 6). This amount of oil was trapped due to the development of fingerings and the capillary effect.

In Figure 6, the lower and intermediate oil saturations correspond to the film-form of trapped oil and the high saturation of oil represents the oil droplets.

3.2 Experiment with packed sand column

The experiments on polystyrene and borosilicate beads have shown the internal structure of the porous model and the saturation distribution of phases in space and time. It was even possible to see the beads of 0.6 mm diameter with the spatial resolution of MRI tool of 0.19 mm for 1 pixel. Unfortunately, this size of grains of porous medium does not allow for the capillary forces to be important because of the large diameter of the pores. To study the simultaneous effect of the viscous, capillary and gravity forces, we have to reduce the grain size and also use some particle-size distribution. For this purpose, we used silica sand, and the experiments were done at different injection rates (0.08, 0.12 and 0.16 mL/min). The concentration of the manganese chloride was increased two times (0.02 mol/L) due to the small adsorption effect of the sand on the solution.

Reference images of the sand model were acquired before starting the experiments in order to check its compatibility with our imaging protocols. As the impact of the system on the signal and especially on the relaxation times was not too important, the sand model was deemed acceptable. The sand was compacted using a vibrating table, and an estimation of the porosity and the permeability was done.

The oil extraction by water flooding in the packed sand model was performed with the same injection rates than in the polystyrene bead model, i.e. 0.08, 0.12 and 0.16 mL/min. The experiments were repeated several times for each rate to check reproducibility.

A series of twelve consecutive images with an interval of 15 minutes is shown in Figure 7 from the first water appearance in FOV (i.e. 1 h 50 after the start of water injection). The shape and the growth of fingers can be clearly observed in these pictures. The first fingers appear in the local micro imperfections of the sand model. Then, they slowly grow in space with help of the capillary forces. The next breakthrough of the fingering happens only when the water saturation on the front reaches a sufficient value. New fingers then appear and start to grow. An alternation between the capillary penetration and the appearance of a new viscous finger was observed. The time between these alternations depends on the injection rate and the model permeability.

The vertical and horizontal cross-sections from Figure 7 show that the loss of connectivity of the oil phase between the water fingers leads to the formation of the trapped oil. For this experiment the final residual oil saturation after injection of 3 pore volumes of water equals to 11%.

To better understand the mechanism of the pulsating movements observed on the condition of slow water pumping, a series of pictures is given in Figure 8.

The difference between the signals of two consecutives images highlights the evolution of the two phases. Figure 8e corresponds to the difference of signal for images (a) and (b). Here, the intensity of the grey colour shows the part of the front where the changes in the saturation happen. In contrary to the polystyrene packed-beads, the saturation change for the sand model occurs on the perimeter of the larger fingers caused by capillary imbibition. The filled grey areas correspond to the emergence of a new finger caused by the viscous force. For this experiment the average flow velocity is of the order of 1.0E−5 m/s

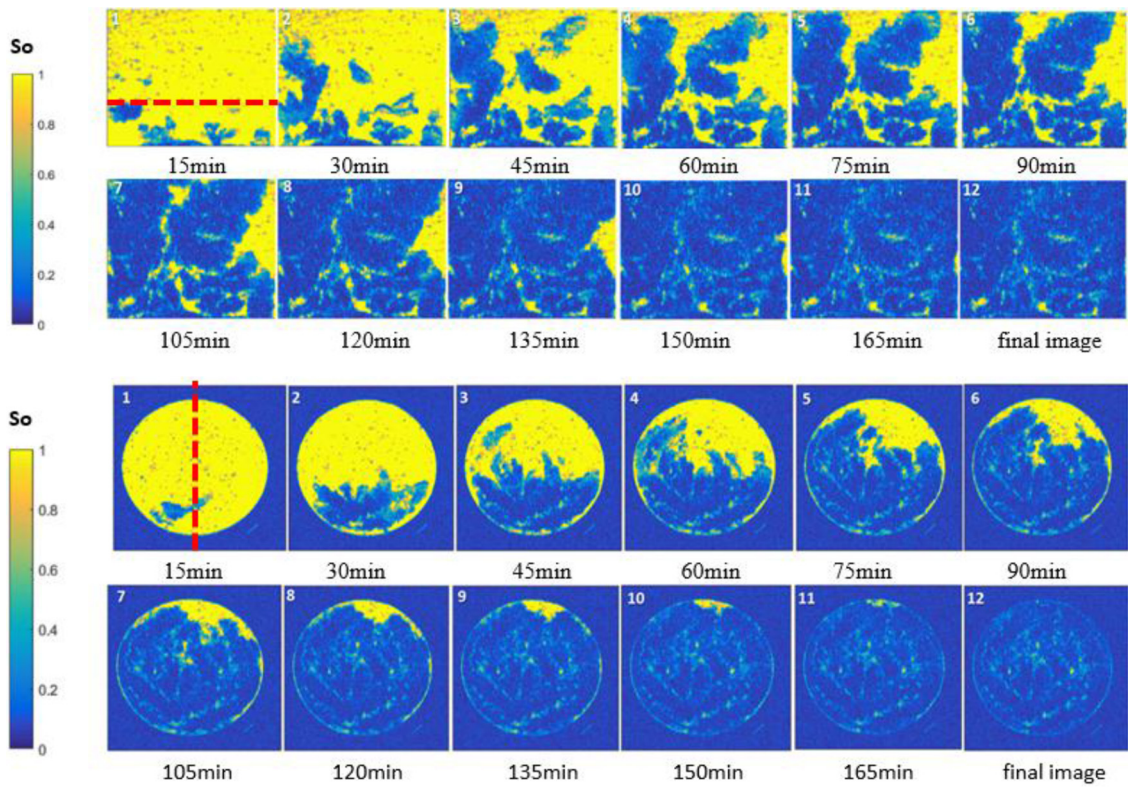

Fig. 7. Consecutive MRI images of the water–oil displacement in the model of packed sand column with the injection flow rate of 0.12 mL/min. The oil is yellow and the water is blue. The time interval between each image equals 15 minutes from the first water appearance in FOV. The dotted line on the first vertical section indicates the position of the horizontal sections (and vice-versa for the horizontal section below).

(estimated from injection rate and taking into account the volume of residual oil). Based on Figure 8f, the averaged velocity of front diffusion in any direction was estimated as 1.0E−6 m/s. It means that the axial redistribution of water is slower than the average flow velocity in vertical direction.

The water flooding experiments on sand were made with different flow rates. The observed process was similar, with difference in the size of the fingers and the interval of alternation with the capillary penetration. Saturation profiles along the vertical axis were reconstructed from vertical images for each acquisition step.

Figure 9 shows the saturation profiles of oil phase recorded at regular intervals (15 min) during the experiments at three different flow rates. At lower injection rate (Fig. 9a), the average saturation in vertical direction increases more monotonously comparing with higher injection rate (Fig. 9b). When the injection rate increases twice (Fig. 9c), the displacement is quite stable and seems to be piston like.

Table 4 summarizing the average residual oil saturation for each case, remaining oil saturation is much lower than polystyrene beads model due to the wettability effect (water-wet). Each experiment was repeated to confirm the obtained results. The oil saturation results ranged from around 10% to 14% at three different injection rates. The residual oil saturation for the various injection flow rate is quite in the same magnitude with a slight increase for the cases of slow displacement.

Figure 10 shows the histogram of the residual oil saturation of the sand model. The maximum values observed for the oil saturation at the final stage is around 0.6, which is different from the polystyrene model (Fig. 6) where the range can reach 1, due to the remaining of big droplets of trapped oil.

The averaged oil saturation as a function of time was calculated through the pore volume (PV) of the model and is presented in Figure 11.

Most experiments with low injection rate show the stabilization of oil saturation up to S_{or} after 1.5–2 of PV injected, and for the rapid displacement one PV injected was enough to replace the mobile oil.

4 Discussion

In order to investigate the interaction of viscosity, gravity and capillary forces on oil displacement mechanism and residual oil saturation, the experimental results of the sand model are analysed using proper dimensionless numbers.

4.1 Dimensionless groups

In fluid dynamics theory, the following main dimensional groups are usually suggested to compute the relative

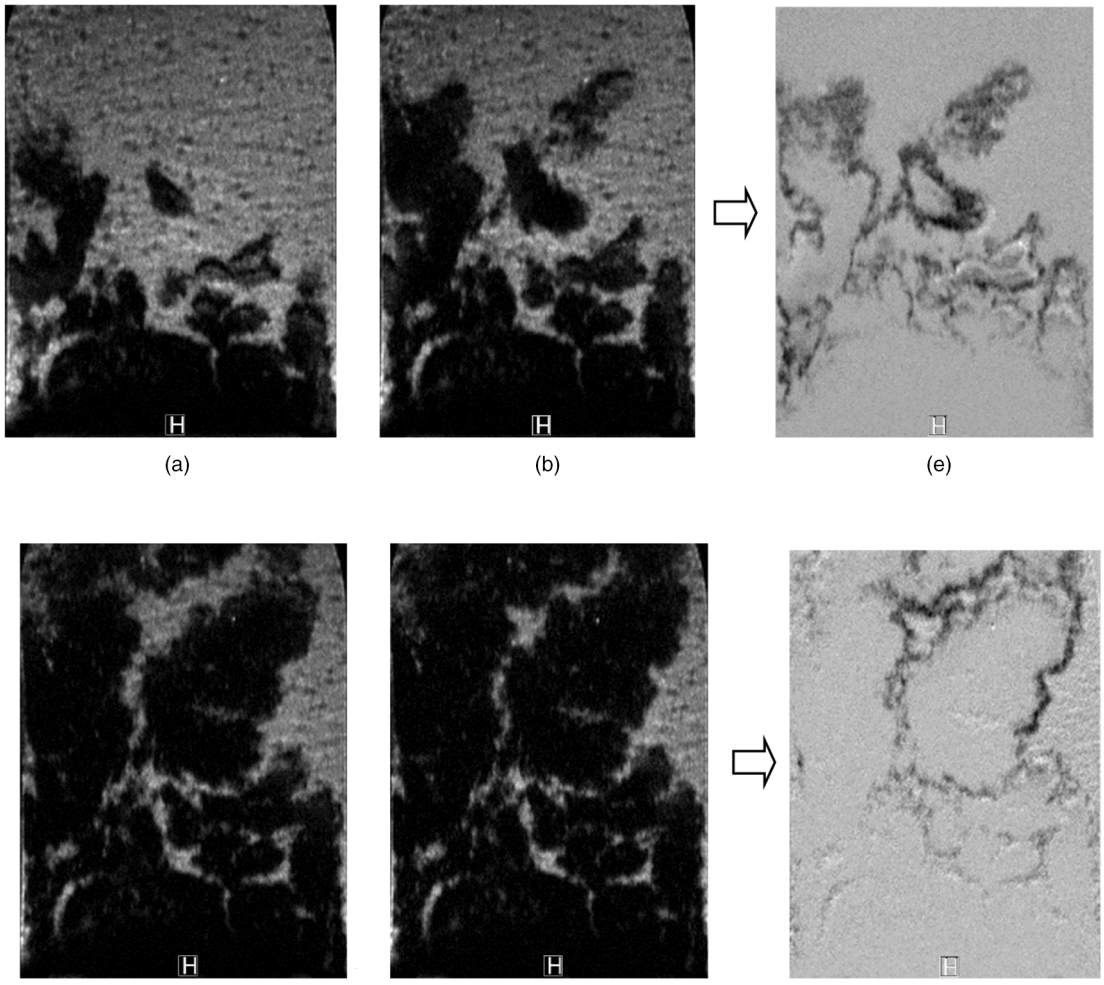

Fig. 8. Oil–water displacement in the sand model, $Q_{inj} = 0.12$ mL/min: (a–d) consecutive images of fingers growth with an interval of 15 minutes; (e): difference between images (a) and (b). (f): difference between images (c) and (d). These two images of saturation difference show the local area where the displacement happens.

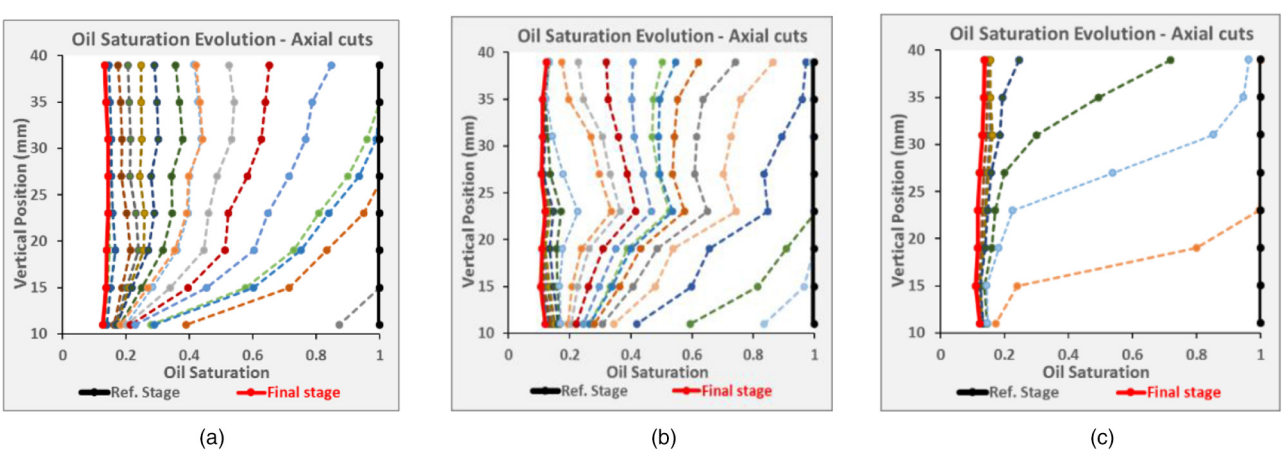

Fig. 9. Oil saturation distribution in the packed sand model at different injection flow rates: (a) 0.08 mL/min, (b) 0.12 mL/min and (c) 0.16 mL/min.

Table 4. Residual oil saturation at different injection rates for the packed sand model.

Q_{inj} (mL/min)	0.08	0.12	0.16
S_{or} (series 1)	13.8%	11.3%	11.8%
S_{or} (series 2)	13.9%	9.7%	12.3%

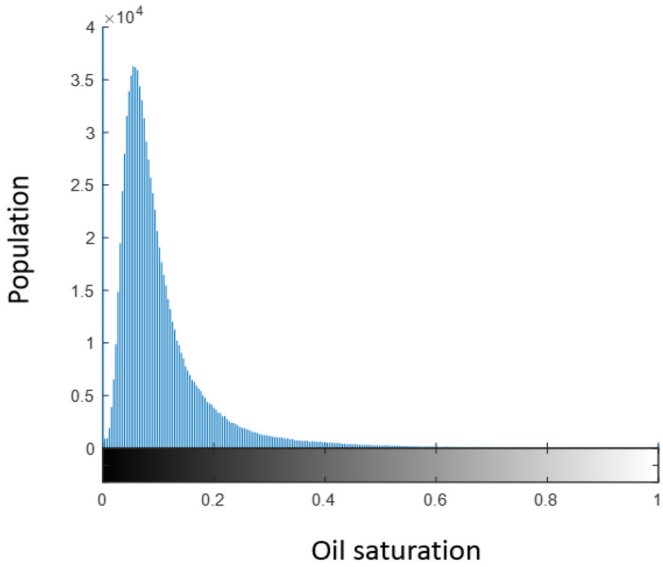

Fig. 10. Histogram of residual oil distribution corresponding to its population in sand beads model (Q_{inj} 0.12 mL/min).

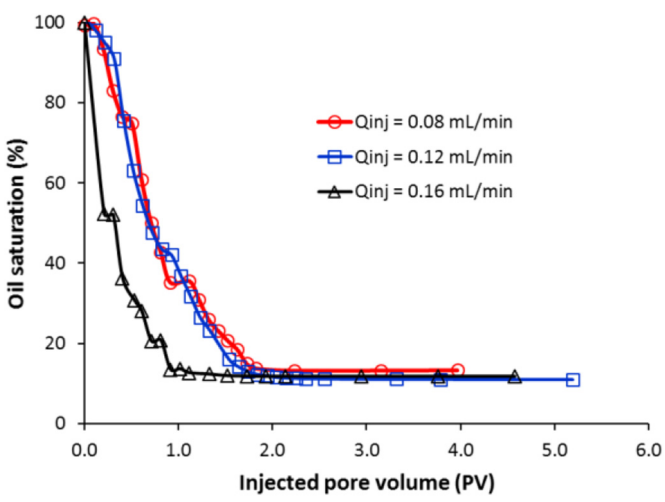

Fig. 11. Averaged oil saturation vs injected PV for the model of packed sand.

magnitudes of the prevailing forces in water flooding processes:

(I) Capillary number (Ca) which is defined as the ratio of the viscous forces to the capillary forces at pore scale and it is expressed as [17]:

$$Ca = \frac{d^2 v \mu_w}{K \sigma \cos\theta} \tag{4}$$

Table 5. Capillary number vs residual oil saturation at different injection rates for sand models.

Q_{inj} (mL/min)	0.08	0.12	0.16
S_{or} (series 1)	13.8%	11.3%	11.8%
Ca	6.41E–06	9.61E–06	1.28E–05

where μ_w is the wetting-phase viscosity, $\boldsymbol{v}$ is Darcy velocity of the injected phase through porous medium (water injection rate divided by the cross-sectional area of the porous medium), K is the intrinsic permeability, σ is the interfacial tension between wetting and non-wetting phases, θ is the contact angle and d is the average pore size. And (II) the Bond number (Bo) which is defined as the ratio of buoyancy forces to capillary forces:

$$Bo = \frac{\Delta \rho g d^2}{\sigma \cos\theta} \tag{5}$$

where $\Delta\rho$ is the difference of density between the two fluids and g is the gravity acceleration.

The pore size d can be calculated as the hydraulic diameter deduced from the average grain diameter dp and the porosity φ:

$$d = \frac{2\varphi}{3(1-\varphi)} d_p. \tag{6}$$

In the following, the residual oil saturation from each sand experiment are analysed using the above-mentioned groups, taking into account different injection rates.

The capillary number is an important parameter to determine the stability of water displacement process. For low capillary number, less than 10E−5, flow is dominated by capillary forces [18]. Somewhat surprisingly, the result at low flow rate has showed (Tab. 4) a slight increase of the residual oil. Table 5 shows the relationship between the capillary number (Ca) and residual oil saturation (S_{or}) at different water injection rates. At low flow rate the capillary number decreases which can explain the increase of residual oil trapped in the porous medium because of capillary fingers growth.

The experiments on sands with dominated capillary forces, $Q_{inj} = 0.08$ mL/min, have demonstrated a little lower "washing effect" for the displacement of oil. It confirms the contribution of the viscous forces on the displacement process at higher capillary numbers.

As for the Bond number, it becomes important when the buoyancy forces are noticeable. This condition requires a vertical direction of flow and a variation in fluid density between wetting and non-wetting phases, which is the case in our experiments.

The results show that in sand model experiments, the Bond number is equal to $Bo = 1.26$E–04. It is the same for all cases of sand models because there are no changes in fluid properties nor grain size. The gravitational forces are therefore relatively small compared to those of capillarity in our experiments.

Both Ca and Bo numbers confirm the important effect of the capillary phenomena. Therefore, the oil displacement largely depends on the capillary forces in the porous medium.

4.2 Displacement mechanism and wettability effect

The three displacement forces of gravity, viscosity and capillarity can act as stabilizing or destabilizing forces of the displacement front depending on the case study. In our case, the properties of the different fluids used remain constant, especially with regards to the viscosity and the density. The viscosity contrast between the two fluids (2.9 cP for oil and 1 cP for water) is not very high, which makes it possible to suppose that initially the viscous effects are not dominant. Furthermore, the direction of the main flow is opposite to the gravity. Thus, the gravity forces would tend to oppose the development of the fingerings along the model and to stabilize the displacement of the moving front. However, the MRI images of the experiments show that the flow is not in the form of a piston and generates fingerings of different scales.

If the capillarity effects are negligible (which is not the case here at all), as it has long been known [19], the displacement front is unstable when the injection velocity is greater than a critical value whose estimation is:

$$v_c = \frac{Kg(\rho_w - \rho_0)}{\varphi(\mu_0 - \mu_w)} \tag{7}$$

For experiments with sand, this critical velocity is about $0.040\,\mathrm{mm\,s^{-1}}$ calculated from the data in Tables 1 and 2. As for the injection rates, they lead to interstitial velocities between 0.0038 and $0.0075\,\mathrm{mm\,s^{-1}}$ below the critical value. However, the intrinsic permeability estimated here from the Kozeny-Carman formula (Eq. (1)) has an uncertainty. Given the fairly large grain size distribution, it is likely that the intrinsic permeability is much lower than $K = 1.5\mathrm{E}{-11}\ \mathrm{m}^2$ estimated in Table 1. It is therefore likely that the displacement of the oil by the water in our experiments might result in viscous fingerings.

In order to settle the question, one can refer to the phase diagram proposed by Lenormand et al. [20,21] connecting the viscosity ratio to the capillary number. The values log $(\mu_\omega/\mu_o) = 0.47$ and log $(Ca) \sim -5$ confirm that the experiments are located at the crossing between stable displacement and capillary fingering.

Moreover, even if the porous medium was prepared in homogenous way, the local heterogeneities on micro-scale cause the appearance of fingers and non-symmetry in horizontal sections (Fig. 7). Nevertheless, the destabilizing effect of viscous difference cannot be compensated by gravity or capillarity forces. Finally, the forces that have a large impact of the water flooding process and developing fingers are mainly the capillary forces, but to a lesser degree the viscosities difference between the two fluids.

The oil-wet and water-wet porous media have been tested. In the oil-wet pores (polystyrene beads), oil is the wetting phase, so that the polystyrene beads will prefer contact with the oil rather than water. In such a configuration, the capillary force acts as a resistance force that prevent oil movement and preserve it in contact with beads surface. The calculation gives $-4.7 < \log(Ca) < -4.4$ with log (μ_ω/μ_o) unchanged, which proves that the situation is not fundamentally modified for the phase diagram compared to that of sand.

Conversely in water-wet pores (packed sand), oil is the non-wetting phase, and the capillary force no longer acts as a resistance force, but as the positive contribution for the momentum balance. Consequently, in our experimental results we can observe that the remaining oil in the oil-wet medium is approximately three times greater than the water-wet medium, S_{or} is 38% for polystyrene beads and 11% for sand at the same experimental conditions. Nevertheless, the oil displacement process in sand model is also impacted by the sample permeability and the capillary forces as the pore size is smaller than in polystyrene model, d is 2.36E−04 m comparing with 4.03E−05 m for sand model (Eq. (6)).

5 Conclusions

High-resolution MRI technique was used to investigate two-phase fluids flow of oil and water in porous media. In this study, experiments were conducted on a vertical porous medium formed from packed polystyrene beads or sand (two materials with different wetting properties). Positive impact on the imaging procedure was observed by adding $MnCl_2$ to the injected water phase. It has shortened the T_2 of water relaxation time to 0.7 ms instead of 2.35 s without any effect on the T_2 of the oil phase. Given the relatively slow displacement of the phases involved (more than 10 hours for an experiment), the MRI technique has allowed us to have a near 3D and highly accurate description of fluid movements.

We emphasize that MRI technique is well adapted to distinguish the distribution of fluids in comparison with other imaging modalities because it only "see" the ^{1}H in liquid phase.

The importance of water channelling or fingering phenomena was obviously found. Obviously the size of the beads/grains and the value of porosity play an important role in the deformation of the moving front. The relationship between the residual oil saturation and dimensionless numbers were also investigated. The water-oil displacement process and the amount of trapped oil are mainly controlled by the wettability of matrix and capillary force. In this study, the flooding process gives the following dimensionless number: $6.4\mathrm{E}{-6} < Ca < 3.8\mathrm{E}{-5}$ and $1.2\mathrm{E}{-4} < Bo < 2.5\mathrm{E}{-3}$, which confirms the important effect of the capillarity.

The flooding images (Fig. 8) have shown that the advance of the displacement front happens in the form of occasional jumps and is controlled by the viscous and capillary forces but also by the heterogeneity of the medium. The analysis of the results based on the phase diagrams proposed by Lenormand [21] confirms that the experiments are located at the intersection of the stable viscous displacement and capillary fingering regimes, which explains that relatively small amplitude fingers are observed.

In this work we pay more attention to the analysis of the phase distribution in the media with the different wettability. As we discussed it at the beginning of the present work, it is not enough to have only a phase saturation value to determine the phase distribution structure in the porous medium. Carrying out these experiments and measuring the trapped oil saturation, we have noticed that the different wettability of the porous medium leads to the different configurations of the interfacial front. In our experimental study the configuration of the interface in form of menisci corresponds to the water wetting medium, presented by the sand models. For this medium, the capillary forces applied to the menisci have the same direction of action as the flow velocity and they contribute into the momentum balance in vectoral form.

For the case of the phase distribution in space in form of films, the capillary forces appear as the pressure difference between the phases, so they don't contribute in the balance of movement, but they play the important role in the trapping process. This case was presented by the oil wetting medium with polystyrene beads. So, the film-form configuration of the phase distribution in space leads to the big amount of oil trapped on the pore surface. The knowledge about the wettability and the size of pore space helps to determine the interfacial front configuration during the two-phase displacement, and better understand the trapping mechanisms for these media.

Nomenclature

Symbols	Descriptions
B_o	Bond number (–)
C	Kozeny-Carman constant (–)
C_a	Capillary number (–)
d	Average pore size (Mm)
d_p	Particle diameter (Mm)
f	Resonance frequency (Hz)
FOV	Field of view (Cm)
g	Gravitational constant ($\mathrm{m\,s^{-2}}$)
^1H	Number of protons (–)
I	Observed magnetic intensity (–)
I_0	Intrinsic magnetic intensity (–)
I_{ref}	Reference MR signal intensity (–)
K	Intrinsic permeability ($\mathrm{m^2}$)
PV	Pore volume ($\mathrm{m^3}$)
Q_{inj}	Injection rate ($\mathrm{mL\,min^{-1}}$)
S_o	Saturation of oil phase (%)
T_E	Echo Time (S)
T_R	Repetition time (S)
T_1	Longitudinal relaxation time (S)
T_2	Transverse relaxation time (S)
v	Darcy velocity of injected phase ($\mathrm{m\,s^{-1}}$)
φ	Sample porosity (%)
ρ_o	Density of oil phase ($\mathrm{kg\,m^{-3}}$)
ρ_w	Density of wetting-phase ($\mathrm{kg\,m^{-3}}$)
$\Delta\rho$	Density difference ($\mathrm{kg\,m^{-3}}$)
μ_o	Oil viscosity (cP)
μ_ω	Wetting-phase viscosity (cP)
σ	Interfacial tension ($\mathrm{N\,m^{-1}}$)
θ	Contact angle (Deg)

This work is supported by LEMTA (Laboratoire d'Energétique et de Mécanique Théorique et Appliquée, UMR 7563) and partially financed by TOTAL.

References

[1] S. Akin, A.R. Kovscek, Computed tomography in petroleum engineering research, in Application of X-ray computed tomography in the geosciences, Geol. Soc. Lond. Spec. Publ. **215**, 23–38 (2003)

[2] F. Larachi, R. Hannaoui, P. Horgue, F. Augier, Y. Haroun, S. Youssef, E. Rosenberg, M. Prat, M. Quintard, X-ray microtomography and pore network modeling of single-phase fixed-bed reactors, Chem. Eng. J. **240**, 290–306 (2014)

[3] T. Pak, I.B. Butler, S. Geiger, M.I.J. Van Dijke, K.S. Sabie, Droplet fragmentation: a new pore-scale process, Proc. Natl. Acad. Sci. **112**, 1947–1952 (2015)

[4] D. Bernard, 3D quantification of pore scale geometrical changes using synchrotron computed microtomography, Oil Gas Sci. Technol. **60**, 747–762 (2005)

[5] S. Chen, K.-H. Kim, F. Qin, A.T. Watson, Quantitative NMR imaging of multiphase flow in porous media, Magn. Reson. Imag. **10**, 815–826 (1992)

[6] Y. Zhao, Y. Song, Y. Liu, H. Liang, B. Dou, Visualization and measurement of CO_2 flooding in porous media using MRI, Ind. Eng. Chem. Res. **50**, 4707–4715 (2011)

[7] Y. Zhao, Y. Song, Experimental investigation on spontaneous counter-current imbibition in water-wet natural reservoir sandstone core using MRI, Magn. Reson. Chem. **55**, 546–552 (2016)

[8] J. Mitchell, T.C. Chandrasekera, D.J. Holland, L.F. Gladden, E.J. Fordham, Magnetic resonance imaging in laboratory petrophysical core analysis, Phys. Rep. **526**, 165–225 (2013)

[9] M. Li, L. Romero-Zerón, F. Marica, B.J. Balcom, Polymer flooding enhanced oil recovery evaluated with magnetic resonance imaging and relaxation time measurements, Energy Fuels **31**, 4904–4914 (2017)

[10] M.L. Johns, L.F. Gladden, Magnetic resonance imaging study of the dissolution kinetics of octanol in porous media, Colloid Interface Sci. **210**, 261–270 (1999)

[11] G. Ersland, M.A. Fernø, A. Graue, B.A. Baldwin, J. Stevens, Complementary imaging of oil recovery mechanisms in fractured reservoirs, Chem. Eng. J. **158**, 32–38 (2010)

[12] W. Salameh, S. Leclerc, D. Stemmelen, J.M. Escanye, NMR imaging of water flow in packed beds, diffusion-fundamentals.org **14**, 1–5 (2010)

[13] I. Panfilova, M. Panfilov, Phenomenological meniscus model for two-phase flow through porous media, Transp. Porous Media **58**, 87–119 (2005)

[14] S. Zeppieri, J. Rodriguez, A.L. Lopez de Ramos, Interfacial tension of alkane + water systems, Chem. Eng. J. **46**, 1086–1088 (2001)

[15] J. Fannir, S. Leclerc, I. Panfilova, D. Stemmelen, Two-Phase displacement in porous media studied by MRI techniques, in

16th European Conference on the Mathematics of Oil Recovery, 2018, pp. 1–13

[16] J. Yan, X. Luo, W. Wang, F. Chen, R. Toussaint, J. Schmittbuhl, G. Vasseur, L. Zhang, Testing oil saturation distribution in migration paths using MRI, J. Petrol. Sci. Eng. **86–87**, 237–245 (2012)

[17] G. Løvoll, Y. Meheust, K. Jørgen Maløy, E. Aker, J. Schmittbuhl, Competition of gravity, capillary and viscous forces during drainage in a two-dimensional porous medium, a pore scale study, Energy **30**, 861–872 (2005)

[18] M.J. Blunt, Multiphase Flow in Permeable Media, Cambridge University Press, 2017

[19] C. Marle, Cours de production, Les écoulements polyphasiques en milieu poreux, tome 4, Technip, 1972

[20] R. Lenormand, E. Touboul, C. Zarcone, Numerical models and experiments on immiscible displacements in porous media, J. Fluid Mech. **189**, 165–187 (1988)

[21] R. Lenormand, Liquids in porous media, J. Phys.: Condens. Matter **2**, 79–88 (1990)

Cite this article as: J. Fannir, I. Panfilova, S. Leclerc, D. Stemmelen, Studying of parameters of two-phase displacement in porous media with MRI technique, Mechanics & Industry **21**, 524 (2020)